

# Nonlinear resonant behavior of a dispersive readout circuit for a superconducting flux qubit

Janice C. Lee,<sup>1</sup> William D. Oliver,<sup>2</sup> Karl K. Berggren,<sup>2,\*</sup> and T. P. Orlando<sup>1</sup>

<sup>1</sup>*Department of Electrical Engineering and Computer Science, Massachusetts Institute of Technology, Cambridge, Massachusetts 02139, USA*

<sup>2</sup>*MIT Lincoln Laboratory, 44 Wood Street, Lexington, Massachusetts 02420, USA*

(Received 14 September 2006; revised manuscript received 17 January 2007; published 11 April 2007)

A nonlinear resonant circuit comprising a SQUID magnetometer and a shunting capacitor is studied as a readout scheme for a persistent-current qubit. The flux state of the qubit is detected as a change in the Josephson inductance of the SQUID magnetometer, which in turn mediates a shift in the resonant frequency of the readout circuit. The nonlinearity and resulting hysteresis in the resonant behavior are characterized as a function of the power of both the input drive and the associated resonance-peak response. Numerical simulations based on a nonlinear circuit model shows that the observed nonlinearity is dominated by the effect due to an ac flux rather than current bias through the Josephson inductor.

DOI: [10.1103/PhysRevB.75.144505](https://doi.org/10.1103/PhysRevB.75.144505)

PACS number(s): 03.67.Lx, 05.45.-a, 85.25.Dq, 85.25.Cp

## I. INTRODUCTION

Superconducting Josephson junction circuits are promising candidates for realizing a quantum computer. These solid-state qubits can be fabricated using standard integrated-circuit techniques. The possibility to incorporate the control and readout circuitry on chip provides a manageable option for scaling up to a larger number of qubits. Quantum-coherent phenomena<sup>1</sup> have been studied utilizing the quantum states<sup>2</sup> of single-qubit circuits and cavities, including superpositions of distinct macroscopic states,<sup>3,4</sup> time-dependent Rabi oscillations,<sup>5–11</sup> cavity quantum electrodynamics,<sup>12–14</sup> and Mach-Zehnder-type interferometry.<sup>15–17</sup> Coherent oscillations,<sup>18</sup> spectroscopic evidence for entanglement,<sup>19</sup> and a prototypical gate operation<sup>20</sup> have also been demonstrated in superconducting coupled qubits. However, to further increase the coherence times of these qubits for manipulation of their quantum states, one must find ways to reduce the amount of noise intrinsic to the qubit, as well as noise introduced by the readout process itself. In particular, several previous readout methods have relied on the switching of a Josephson circuit from a zero-voltage to a finite-voltage state. This switching generates quasiparticles, and thus such a readout approach is limited by the subsequent decoherence. More recently, dispersive readout schemes have been developed such that the qubit is coupled to a resonator, and the state of the qubit is detected as a shift in the resonant frequency of the resonator. As a result, the readout process requires only lower input biases and hence minimizes the generation of quasiparticles. Furthermore, the resonator also acts as a narrow-band filter, which shields the qubit from broadband noise. Dispersive readout has been implemented for the persistent current qubit,<sup>21,22</sup> for the charge qubit,<sup>23</sup> and for the hybrid qubit where the readout was operated in the nonlinear regime for its use as a bifurcation amplifier.<sup>24</sup>

This paper focuses on characterizing the nonlinear resonant behavior of the dispersive readout circuit for a persistent current qubit. The readout element is a SQUID magnetometer, which is operated as a nonlinear, flux-sensitive inductor incorporated in an  $L$ - $C$  resonator. The qubit is coupled to the

SQUID inductor, and the flux state of the qubit is detected as a shift in the resonant frequency of the resonator by means of magnitude and/or phase measurements. Our approach differs from other resonant-type experiments in two main ways. First, our qubit and readout circuit were fabricated on the same chip from niobium, whereas the implementations in Refs. 21–24 were aluminum based. Second, we were able to achieve a high-quality factor for the resonator by incorporating an rf transformation network on chip using the planarized niobium process. We observed resonant behavior due to the nonlinear Josephson inductance of the SQUID, given the high-quality factor of the resonance.<sup>25,26</sup> The frequency spectra of the readout circuit were characterized in both the linear and nonlinear regimes. Biasing the readout circuit in the nonlinear regime potentially provides additional sensitivity for distinguishing the qubit states.<sup>24</sup>

The persistent current (PC) qubit used in this study is a superconducting loop interrupted by three Josephson junctions, two of which have the same critical current while the third junction has a critical current reduced by a factor  $\alpha$ .<sup>27,28</sup> When the external magnetic flux threading the qubit loop is biased near half a flux quantum, the two lowest-energy states correspond to oppositely circulating persistent currents in the qubit loop. The induced flux of the persistent current (and hence the state of the qubit) is detected by a SQUID magnetometer which surrounds the qubit.

In the resonant readout scheme, the SQUID magnetometer is operated based on the property that the Josephson inductance of the SQUID is a nonlinear function of both the current bias  $I_{sq}$  and the flux bias  $\Phi_{ext}$ . In our experiments, the current bias comprises solely an ac component, whereas the flux bias  $\Phi_{ext} = \Phi_{dc} + \Phi_{ac}$  has both a dc component corresponding to the external bias, and an ac component corresponding to the induced flux that is mutually coupled to the SQUID. In particular, we expect that the flux induced by the circulating current in the resonating loop can be coupled to the SQUID, and the size of the coupled flux is significant near the resonant frequency at which the resonating current becomes  $Q$  times the input current drive ( $Q$  enhancement).

To demonstrate the general principles underlying the operation, consider the limiting case where the SQUID has negligible loop inductance and symmetric junctions each with

critical current  $I_{co}$ . In this limit, the SQUID behaves like an equivalent single junction with an effective critical current given by  $I_c(\Phi_{ext}) = 2I_{co}|\cos(\pi\Phi_{ext}/\Phi_o)|$ , and an effective phase given by  $\varphi_p = \sin^{-1}[I_{sq}/I_c(\Phi_{ext})]$ . By defining the Josephson inductance according to  $V_{sq} = d[L_J I_{sq}]/dt$ , where  $V_{sq}$  is the voltage across the SQUID, we obtain the inductance to be

$$L_J(I_{sq}, \Phi_{ext}) = \frac{\Phi_o}{2\pi I_c(\Phi_{ext})} \frac{\varphi_p}{\sin \varphi_p}. \quad (1)$$

In the linear regime where the current and flux biases are small, one can approximate the SQUID by a linear inductor given by

$$L_{Jo} = \frac{\Phi_o}{4\pi I_{co}}. \quad (2)$$

The inductance for small ac drives can be approximated quasistatically by the inductance at the dc operating points for the current and flux biases. To demonstrate the separate effects due to the current and the flux, we first set  $\Phi_{ext}$  to zero and reduce Eq. (1) to

$$L_J(I_{sq}, 0) = 2L_{Jo} \frac{\varphi_p}{\sin \varphi_p}, \quad (3)$$

where  $\varphi_p = \sin^{-1}(I_{sq}/2I_{co})$ . Thus, the inductance increases with the size of the driving dc current bias. Likewise, when  $I_{sq}$  in Eq. (1) is set to zero,

$$L_J(0, \Phi_{ext}) = \left| \frac{L_{Jo}}{\cos\left(\frac{\pi\Phi_{ext}}{\Phi_o}\right)} \right|, \quad (4)$$

which has a periodic dependence on the dc flux bias with periodicity given by  $\Phi_o$ . Starting from a bias of  $\Phi_{dc} = 0$ , the inductance increases with flux, and starting from a bias of  $\Phi_{dc} = 0.5\Phi_o$ , the inductance decreases with flux.

The general trend of an ac bias can be conceptualized as averaging the inductance about the dc bias point over the range of the ac bias. Hence, near  $\Phi_{dc} = 0$  both the ac driving current and the ac flux increase the effective inductance as the ac drives increase. In contrast, near  $\Phi_{dc} = 0.5\Phi_o$  an increasing ac flux bias tends to decrease the effective inductance and an increasing ac current bias tends to have the opposite effect. Therefore, the current and flux act in concert at  $\Phi_{dc} = 0$ , whereas, they compete at  $\Phi_{dc} = 0.5\Phi_o$ . From our experiments and numerical simulations,<sup>29</sup> we have found in our readout circuit that the ac flux dominates at  $\Phi_{dc} = 0.5\Phi_o$ . Consequently, this paper will focus on the effects due to flux, thereby allowing us to develop a nonlinear LRC model that qualitatively matches the experimental observations.

Figure 1(a) shows the circuit schematic of the resonant readout circuit. The PC qubit is mutually coupled to the SQUID inductor  $L_J$ . The resonating loop comprises  $L_J$ ,  $L_2$ , and the parallel combination of  $C_1$  and  $C_2$ . To raise the quality factor of the resonance for higher readout sensitivity, a tapped-inductor transformer formed by  $L_2$  and  $L_J$  is used to step up the effective output resistance at the resonant frequency. On the input side,  $L_1$  and  $C_1$  form an  $L$ -match net-

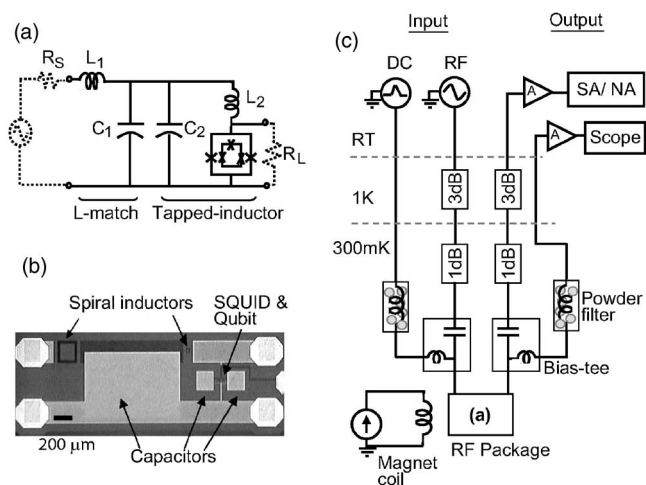


FIG. 1. Experimental setup: (a) Circuit schematic of the resonant readout circuit. The designed component values were  $L_1 = 69$  nH,  $L_2 = 0.78$  nH,  $C_1 = 1.4$  pF, and  $C_2 = 100$  pF. The SQUID inductance  $L_J$  was approximated to be 0.1 nH for the circuit design.  $R_S$  and  $R_L$  were 50  $\Omega$  impedances. (b) Optical micrograph of the actual device. (c) Electronic setup at different temperature stages of the  $^3\text{He}$  cryostat.

work, which matches the input resistance to the transformed output resistance.<sup>30</sup>  $R_S$  and  $R_L$  represent the 50  $\Omega$  source and load impedances from the RF electronics, and no resistors were fabricated on chip. The junctions of the SQUID are each shunted by a 5 pF capacitor (not shown).

The device was fabricated using the planarized niobium trilayer process at MIT Lincoln Laboratory.<sup>31</sup> A device micrograph is shown in Fig. 1(b). The Josephson critical current density was estimated to be 1.2  $\mu\text{A}/\mu\text{m}^2$  from the process test data. The Josephson junctions were laid out as squares with a dimension of 1.0  $\mu\text{m}$  and 0.9  $\mu\text{m}$  for the qubit, and 1.5  $\mu\text{m}$  for the SQUID. Due to process bias, the effective electrical junction dimensions are expected to be smaller. We measured the effective size of the SQUID junctions to be approximately 1.3  $\mu\text{m}$ , a reduction of 0.2  $\mu\text{m}$  from their drawn dimension. The effective qubit junction sizes were not measured directly, but were estimated to have a reduction of approximately 0.35  $\mu\text{m}$ , as determined by measuring similarly drawn 1.0  $\mu\text{m}$  process-test junctions nearby. The area ratio of the SQUID to the qubit loop was designed to be 1.3, with mutual coupling estimated to be 30 pH. The inductors were realized by square spirals with a linewidth and spacing of 1  $\mu\text{m}$ , while the capacitors comprised Nb electrodes with a dielectric consisting of 50 nm of  $\text{Nb}_2\text{O}_5$  and 200 nm of  $\text{SiO}_2$ .

Our measurements were taken in a  $^3\text{He}$  cryostat at 300 mK. The measurement setup is shown in Fig. 1(c). The dc lines were used to characterize the properties of the Josephson junctions, while the rf lines were used for the resonant readout. The dc lines were filtered by copper powder filters at 300 mK, whereas the rf lines had 3 dB attenuators at the 1 K stage and 1 dB attenuators at the 300 mK stage. The choice of attenuation was less than what was ideal to attenuate the Johnson noise at the various temperature stages, and was determined based on the signal-to-noise ratio

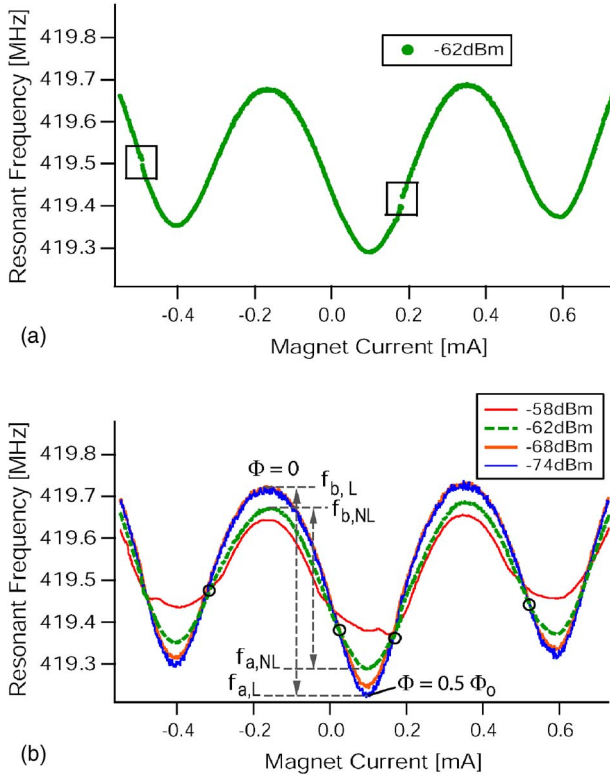


FIG. 2. (Color online) (a) Modulation of the resonant frequency with external dc flux bias. Qubit steps are observed at 0.18 mA and  $-0.495$  mA. (b) Modulation of the resonant frequency for various input power. The amount of modulation is reduced in the nonlinear regime ( $f_{b,NL} - f_{a,NL}$ ) compared to the linear regime ( $f_{b,L} - f_{a,L}$ ). The circular markers represent the inflection points where  $d^2f_o/d\Phi^2=0$ .

of the output, which was measured with a room-temperature amplifier. Larger attenuation can be used in future experiments where a cryogenic amplifier is incorporated. In addition, the external dc flux bias for the qubit was provided by a superconducting coil wrapped around the sample housing. We measured the transmission characteristics of the readout circuit with a spectrum analyzer equipped with a tracking generator, or with a network analyzer when the phase information was needed. We used a resolution bandwidth (RBW) of 3 kHz, and averaged each spectrum 100 times.

## II. QUBIT READOUT AND EFFECT OF INPUT BIAS ON READOUT CIRCUIT

The resonant frequency of the readout circuit was measured to be near 419 MHz, with a quality factor estimated to be on the order of 1000. Figure 2(a) shows the results when an external flux bias  $\Phi_{ext}$  was applied through the sample. At a given  $\Phi_{ext}$ , we measured both the resonant frequency and the peak power of the resonant spectrum. The resonant frequency of the readout circuit, in the linear regime where all the ac biases are small, is related to the effective inductance  $L_J$  and capacitance  $C$  by

$$f_o(\Phi_{ext}) = \frac{1}{2\pi\sqrt{[L_s + L_J(\Phi_{ext})]C}}. \quad (5)$$

For our circuit parameters,  $L_s$  corresponds to the bias resistor  $L_2$ , and  $C$  is given by  $C_1 + C_2 \sim C_2$  in Fig. 1(a).

A periodic modulation of the resonant frequency of the readout circuit was observed and is interpreted as being caused by the periodic modulation of the Josephson inductance of the SQUID. At every 1.3 times the SQUID modulation period, a shift in the resonant frequency, corresponding to about 2 pH (1%) change in Josephson inductance, was observed. These shifts, referred to as qubit steps, represent a qubit transition between oppositely circulating current states, and occur near flux biases of half a flux quantum  $\Phi_q = 0.5\Phi_o$  for the qubit. As the flux is swept past  $\Phi_q = 0.5\Phi_o$ , it is more energetically favorable for the qubit to change from one circulating current state to another in order to stay in the ground state. The resultant change in the induced flux from the qubit loop is coupled to the SQUID and accounts for the discontinuities in the SQUID modulation curve. The periodicity of the qubit steps (corresponding to a flux quantum for the qubit) and the periodicity of the SQUID lobes (corresponding to a flux quantum for the SQUID) are related by the ratio of their loop areas defined by the fabrication parameters. In addition, we observed a dip in the resonance-peak power near the qubit step (not shown), which corresponds to a broadening of the resonant spectrum.<sup>32</sup> Moreover, the paraboliclike background observed in the frequency modulation curve was due to undesired heating from the magnet current in the dc (soft-coax) lines. The heating causes an increase in the resonant frequency, and is more significant at high magnet current biases. The heating effect was eliminated for faster scans and when the sample was later tested in a dilution refrigerator using superconducting magnet leads.

Figure 2(b) shows that as the level of input bias increases, the amount by which the frequency is modulated over a flux quantum decreases. This will be shown in the next section to be a direct consequence of the shape of the resonant spectrum as it becomes increasingly nonlinear with higher input power.

## III. NONLINEAR RESONANT BEHAVIOR OF A READOUT CIRCUIT

The resonant readout circuit can experimentally distinguish the difference in the flux produced by the circulating current states of the qubit. Given that the efficacy of the readout scheme depends on the nonlinear response of the readout circuit, we now characterize the resonant behavior of the readout circuit as a function of the dc flux bias for higher ac drives.

Figure 3 shows the evolution of the magnitude and phase spectra with increasing input power for external flux biases of  $\Phi_{dc} = 0, 0.3\Phi_o$ , and  $0.5\Phi_o$ . In the case when  $\Phi_{dc} = 0$ , the magnitude and phase spectra evolve from a symmetric shape to being asymmetric with a lower resonant frequency as the power of the drive is increased. The lower resonant frequency indicates that the effective Josephson inductance over an oscillating period is higher. For higher levels of the input power, the magnitude spectrum exhibits a discontinuity near the resonant frequency, where the system jumps from the lower branch to the higher branch. The phase spectrum also exhibits a discontinuity similar to the magnitude spectrum. For  $\Phi_{dc} = 0.5\Phi_o$ , the asymmetry is opposite to that of

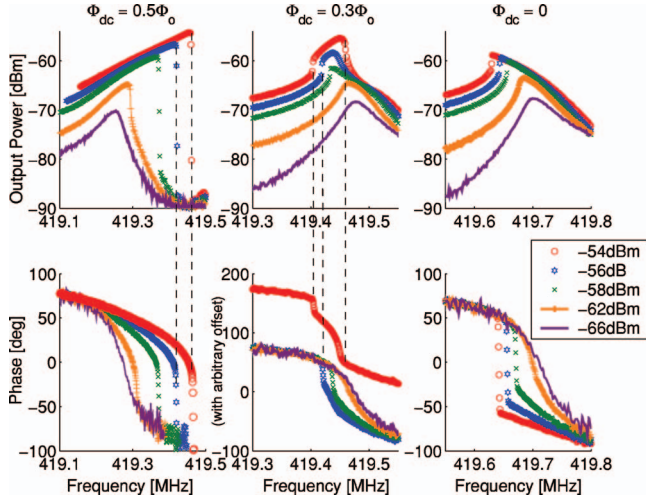


FIG. 3. (Color) Evolution of the magnitude and phase spectra of the readout circuit from the linear to the nonlinear regime with increasing input power. Data are shown for flux biases at  $\Phi_{dc}=0$ ,  $0.3\Phi_o$ , and  $0.5\Phi_o$ . The nonlinear spectrum evolves from having a lower resonant frequency at  $\Phi=0$  to having a higher resonant frequency at  $\Phi=0.5\Phi_o$ . The phase spectrum at  $-54$  dBm for  $\Phi=0.3\Phi_o$  was arbitrarily shifted for display purpose. A self-resonant dip was observed near the resonant frequency of the spectrum, e.g., at 419.5 MHz for  $\Phi_{dc}=0.5\Phi_o$ , and accounted for the general tilt in the shape of the spectrum. The self-resonance is believed to be due to parasitic capacitive coupling between the input and output ports.

$\Phi_{dc}=0$ ; the resonant frequency increases with higher power, indicating that the overall effective inductance is decreasing with increasing power of the drive. An intermediate behavior is captured at  $\Phi_{dc}=0.3\Phi_o$ . As the input power increases, the nonlinear magnitude spectrum first bends towards the lower frequency side, then gradually evolves into a characteristic shape with two discontinuities near the resonant frequency, once when the magnitude is increasing and once when the magnitude is decreasing. Similarly, the phase spectrum also shows two discontinuities at the same frequency locations, with a partial phase drop at each discontinuity.

The shapes of these curves are similar to the response of driven, weakly nonlinear systems, which exhibit an instability region indicating multiple solutions and hysteresis.<sup>33,34</sup> Two such curves are shown in Figs. 4(a) and 4(b). In particular, we model our system as a nonlinear circuit, which results from a current-driven LRC resonant circuit with a nonlinear inductor  $L$ . In this case the flux in the inductor  $\Phi$  satisfies

$$I \sin \omega_s t = C \frac{d^2 \Phi}{dt^2} + \frac{1}{R} \frac{d\Phi}{dt} + h(\Phi, d\Phi/dt), \quad (6)$$

where the function  $h(\Phi, d\Phi/dt)$  models the nonlinearity of the inductor. For example, when  $h = \Phi/L_o$  then the system is a simple LRC resonant circuit with a linear inductor  $L_o$ . When  $h \sim \sin \Phi$  the nonlinear equation is analogous to a driven pendulum system whose response is similar to Fig. 4(b).<sup>33,37,38</sup> Another example is the Duffing equation where  $h \sim \Phi - c\Phi^3$ , whose response is like Fig. 4(a) for negative  $c$  and like Fig. 4(b) for positive  $c$ .<sup>33,34</sup> In Sec. V we will use a

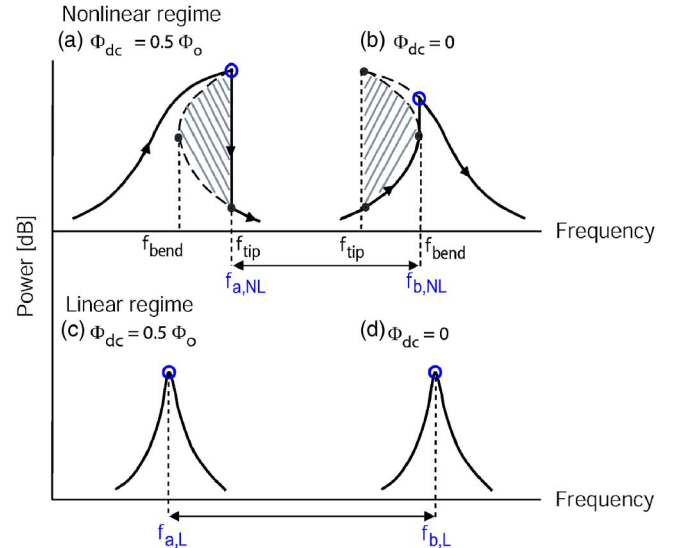


FIG. 4. (Color online) Illustration of the resonant spectra in the nonlinear regime [(a) and (b)] and the linear regime [(c) and (d)] for  $\Phi=0.5\Phi_o$  and  $\Phi=0$ , respectively. The shaded region of the nonlinear spectrum marks the region over which multiple solutions occur. The solid line traces the actual spectrum observed experimentally with a forward frequency sweep, and the circular marker corresponds to the peak frequency that was being measured. The bending of the nonlinear spectra to opposite sides accounts for the reduced separation of resonant frequencies ( $f_{b,NL} - f_{a,NL}$ ) compared to the linear case ( $f_{b,L} - f_{a,L}$ ), as was observed in Fig. 2(b).

functional form for the effective inductance, which incorporates both the needed dependence on applied dc flux and the resonant-frequency dependence observed for small drives. In fact, given that Fig. 2 shows that the resonant frequency is periodic in the applied dc flux, then the effective inductance that needs to be captured in the form of  $h$  must also follow this same periodicity.

We now use the illustration in Fig. 4 to explain some of the general features of the data in Fig. 2 and to motivate the subsequent analysis. In Fig. 4, the shape of the resonant spectra are shown for both the linear and nonlinear regimes for  $\Phi_{dc}=0$  and  $0.5\Phi_o$ , with the resonant frequency at  $\Phi_{dc}=0.5\Phi_o$  lower than at  $\Phi_{dc}=0$  given the flux dependence of the effective inductance. The shaded region of the nonlinear spectrum corresponds to the region  $f \in [f_{tip}, f_{bend}]$  over which multiple solutions occur (two of which are stable and one of which is unstable).<sup>35</sup> The solid line traces the actual spectrum observed experimentally with a forward frequency sweep, and the circular marker corresponds to the peak frequency that was being measured.

We have seen from Fig. 2(b) that as the level of input power increases, the amount by which the frequency is modulated over a flux quantum decreases. This is a direct consequence of the shape of the resonant spectrum as the system response becomes increasingly nonlinear. As illustrated in Figs. 4(c) and 4(d), the resonant spectra at  $\Phi=0$  and  $0.5\Phi_o$  have resonant frequencies that are maximally separated ( $f_{b,L} - f_{a,L}$ ) when the input bias is low, and therefore when the resonant spectra are nearly those of a linear response. As the input current bias increases, the resonant

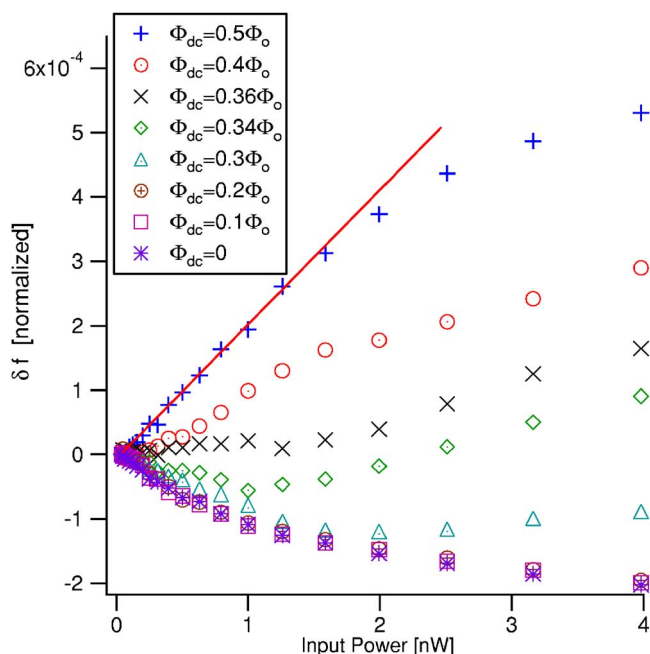


FIG. 5. (Color online) Bending  $\delta f$  as a function of input power from  $-74$  dBm to  $-54$  dBm in 1 dB steps. Measurements were made with a forward frequency sweep. The data are shown for various dc flux biases between 0 and  $0.5\Phi_o$ . The sign of  $\delta f$  indicates the polarity of the asymmetric spectrum. The red line corresponds to a linear fit in the low-power regime.

spectrum evolves from the symmetric Lorentzian shape to an asymmetric shape. This is shown in Figs. 4(a) and 4(b). The fact that the nonlinear spectra bend to opposite sides at  $\Phi=0$  and  $0.5\Phi_o$  accounts for a reduced amount of modulation in resonant frequency ( $f_{b,NL}-f_{a,NL}$ ) compared to the linear case. It was also observed in Fig. 2(b) that the frequency modulation curves for different input power meet periodically at the inflection points, where the second derivative  $d^2f_o/d\Phi^2$  equals zero. In fact, the asymmetry of the spectrum changes sign near the inflection points.

To further quantify the amount of bending in the nonlinear spectrum, we introduce a parameter  $\delta f$  which is a normalized shift of the resonant frequency  $f_n$  of the nonlinear spectrum relative to the linear spectrum  $f_o$ ,

$$\delta f = \frac{f_n - f_o}{f_o}. \quad (7)$$

Experimentally,  $f_o$  was determined as the resonant frequency of the spectrum measured at the lowest power ( $-74$  dBm).  $f_n$  was defined as the peak frequency and, in the limit of high input power, the frequency at which the discontinuity occurs. The sign of  $\delta f$  serves as an indication of the polarity of the bending. A positive  $\delta f$  corresponds to the nonlinear spectrum bending to the higher-frequency side, and a negative  $\delta f$  corresponds to the spectrum bending to the lower-frequency side.

In Fig. 5 the normalized frequency  $\delta f$  of the resonant spectrum is plotted for increasing input power from  $-74$  dBm to  $-54$  dBm. The measurements of the spectra

were made with a forward frequency sweep. The different markers correspond to various flux biases between  $\Phi_{dc}=0$  and  $0.5\Phi_o$ . At  $\Phi_{dc}=0.5\Phi_o$  (top plot),  $\delta f$  is increasingly positive; whereas, at  $\Phi_{dc}=0$  (bottom plot),  $\delta f$  becomes increasingly negative. Furthermore, the amount of bending  $|\delta f|$  at  $\Phi_{dc}=0$  is smaller than at  $0.5\Phi_o$  for a given input bias, which is related to the fact that a forward frequency sweep captures the full frequency extent of the bistable region for  $\Phi_{dc}=0.5\Phi_o$  but not for  $\Phi_{dc}=0$ . (The reverse is true if the frequency is swept backwards, as discussed in the next section.) Finally, at intermediate flux biases between  $0.3\Phi_o$  and  $0.36\Phi_o$ ,  $\delta f$  shows an undulating behavior, corresponding to the asymmetric spectrum constantly varying its polarity. There is an initial linear dependence of  $\delta f$  on input power, which will be discussed in the next section.

#### IV. HYSTERESIS OF THE RESONANT SPECTRUM

For larger input drives, the resonant spectrum exhibits a discontinuity, which corresponds to one of the two boundaries of the bistable region. Within the bistable region, the system settles into one of the solutions depending upon the initial conditions. For our case, the initial condition is set by the solution at the previous driving frequency, which in turn is determined by the direction of the frequency sweep. The resonant behavior of the readout circuit presented so far was obtained with a forward frequency sweep. Here, we present the hysteretic behavior of the resonant spectrum measured with both forward and backward frequency sweeps so that the full boundary of the bistable region can be mapped.

The top three plots in Fig. 6 show the typical hysteretic spectrum for flux biases at  $\Phi_{dc}=0$ ,  $0.3\Phi_o$ , and  $0.5\Phi_o$ . The data are shown for an input power level of  $-54$  dBm, which corresponds to a highly nonlinear regime. The direction of the frequency sweep is indicated by the arrows. For the case of  $\Phi_{dc}=0$  and  $0.5\Phi_o$ , we define the extent of the bistable region as  $|f_t - f_b|$ , where  $f_b$  is the frequency at which the resonant spectrum jumps from the lower to the higher stable branch, and  $f_t$  corresponds to the frequency at which the spectrum falls from the higher to the lower stable branch. At  $\Phi_{dc}=0.3\Phi_o$ , the forward and backward traces overlapped, indicating that the bistable region associated with the two discontinuous edges were too small to be detected given the frequency resolution.

The onset of the hysteretic regime is illustrated in the middle three plots of Fig. 6, where the extent of the bistable region was characterized as a function of input power from  $-66$  dBm to  $-54$  dBm in 1 dB steps. First, we normalized  $f_t$  and  $f_b$  with respect to the resonant frequency  $f_o$  in the linear regime according to a definition similar to Eq. (7).

$$\delta f_t = \frac{f_t - f_o}{f_o} \quad \text{and} \quad \delta f_b = \frac{f_b - f_o}{f_o}. \quad (8)$$

$\delta f_t$  and  $\delta f_b$  were then plotted as a function of input power. Hysteretic behavior was observed when the input bias was above a threshold  $P_H$ , which was measured to be  $-61$  dBm for  $\Phi=0.5\Phi_o$ , and at a higher power of  $-59$  dBm for  $\Phi=0$ .

In the bottom row of plots of Fig. 6, we have plotted  $\delta f_t$  and  $\delta f_b$  as a function of the resonance-peak power. We see

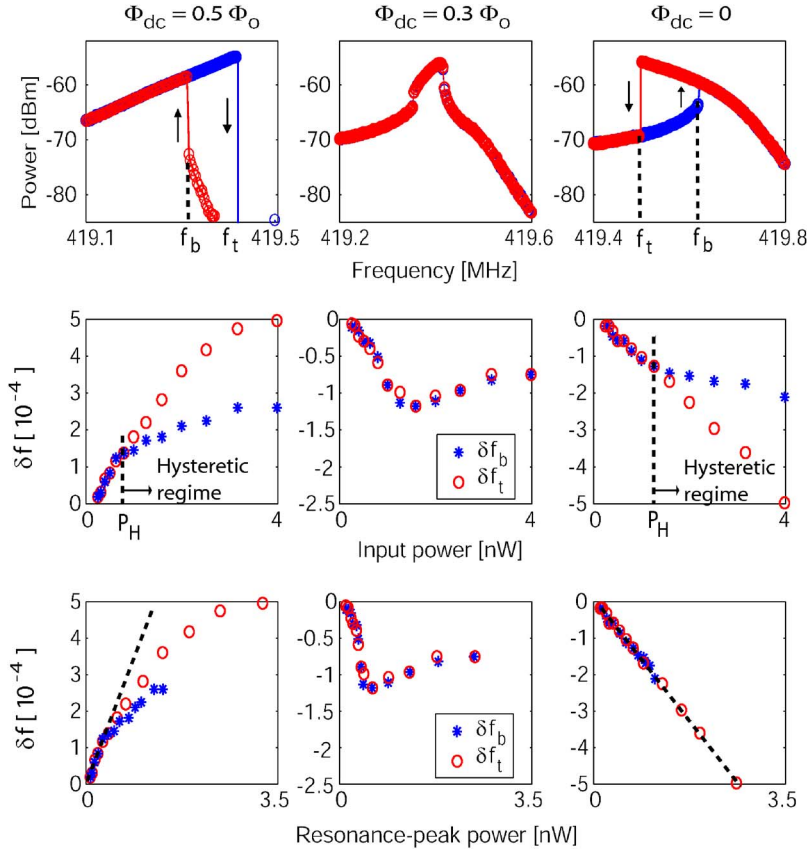


FIG. 6. (Color online) Top plots: Hysteretic resonant spectrum for flux biases at  $\Phi_{dc}=0$ ,  $0.3\Phi_o$ , and  $0.5\Phi_o$ . The extent of the bistable region is given by  $|f_t - f_b|$ . Middle plots:  $\delta f_t$  and  $\delta f_b$  as a function of input power from  $-66$  dBm to  $-54$  dBm in 1 dB steps. The onset of hysteretic regime occurs at  $P_H = -61$  dBm for  $\Phi_{dc} = 0.5\Phi_o$  and  $P_H = -59$  dBm for  $\Phi_{dc} = 0$ . Bottom plots:  $\delta f_t$  and  $\delta f_b$  replotted as a function of resonance-peak power. The dotted line is a linear fit for low power.

that  $\delta f_t$  is initially a linear function of the resonance-peak power for all three fluxes shown and that it is fully linear for zero dc flux. This initial linear dependence on resonance-peak power is found for many functional forms of the nonlinear term  $h(\Phi, d\Phi/dt)$ .<sup>33,34</sup> However, the dependence on input power varies according to the particular functional form of  $h(\Phi, d\Phi/dt)$  (see Ref. 34 for some sample cases). For example, both the Duffing equation and the pendulum model give a linear dependence on both input and resonance-peak powers in the weakly nonlinear regime.<sup>34–36</sup> For  $h = \Phi(d\Phi/dt)^2$ ,  $\delta f_t$  depends linearly on the resonance-peak amplitude, but as the cube root of the input power.<sup>34</sup>

## V. SIMULATIONS OF NONLINEAR RESONANT BEHAVIOR BASED ON AN LRC CIRCUIT MODEL

In this section, we simulate the nonlinear resonant behavior of the readout circuit. One of the approaches to analyze the ac-driven behavior of a circuit comprising a SQUID is to solve the set of coupled differential equations governing the SQUID consistently with the rest of the circuit. However, the dynamical modeling of the resulting circuit is complex; for example, for a circuit with a SQUID shunted by a resonating capacitor has six dynamical variables when the mutual inductive coupling between the SQUID and the resonating loop is included.<sup>29</sup> Here, we present simulation results based on the LRC circuit model of Eq. (6) with the linear inductance replaced by a flux-dependent nonlinear inductor. The circuit schematic is shown in Fig. 7(a). This approach reduces the mathematical complexity of the problem to one

dynamical variable, and at the same time, it models the nonlinearity of the SQUID due to an ac flux bias. The observed nonlinear resonant behavior was qualitatively reproduced.

Specifically, the readout SQUID is modeled by a flux-dependent nonlinear inductor  $L_J(\Phi_{ext})$  given by

$$L_J(\Phi_{ext}) = \frac{L_o}{\sqrt{(1 + \beta^2) + (1 - \beta^2)\cos(2\pi\Phi_{ext}/\Phi_o)}}. \quad (9)$$

The functional form for the nonlinear inductance was motivated by the Josephson inductance of an asymmetric SQUID. Equation (9) has the form of  $L_J(\Phi_{ext}) = \Phi_o / 2\pi I_c(\Phi_{ext})$ , where  $I_c(\Phi_{ext})$  corresponds to the critical current of a SQUID with asymmetric junctions of  $I_{co}(1 \pm \beta)$ .<sup>37</sup> The functional form for the nonlinear inductor  $L_J(\Phi_{ext})$  in Eq. (9) captures the sinusoidallike shape of the frequency response of the actual readout circuit as previously shown in Fig. 2(b). This is illustrated in Fig. 7(b), where  $L_J(\Phi_{ext})$  is plotted for  $L_o = \sqrt{2}L_{Jo}$  [Eq. (2)], and for different values of  $\beta$ . It can be seen that  $\beta$  has an effect on (a) the amount by which  $L_J$  is modulated over half a flux quantum, and (b) the locations of the inflection points at which the second derivative  $d^2L_J/d\Phi^2$  is zero. We used  $\beta$  to fit the locations of the inflection points ( $d^2f_o/d\Phi^2 = 0$ ) in the frequency response data in Fig. 2(b). It should be noted that in this nonlinear LRC circuit model, we have used asymmetry in the junctions as one possible explanation for the shape of the frequency response data. However, regardless of the physical origin of Eq. (9), it is only its functional form that is important in capturing the flux dependence of the inductance.

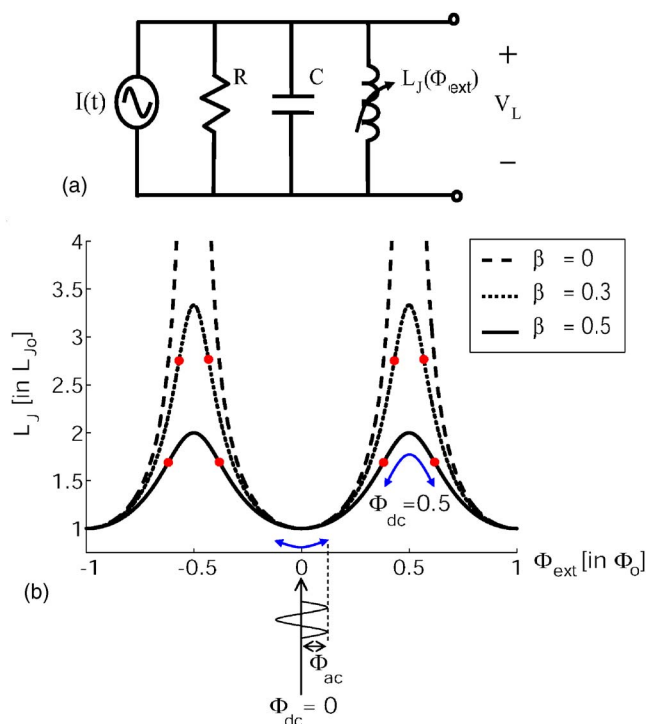


FIG. 7. (Color online) (a) Circuit schematic of the simulated nonlinear LRC circuit model. The circuit is driven by a current source  $I \sin \omega_s t$ . The readout SQUID is modeled by a flux-dependent nonlinear inductor given by Eq. (9). The simulated circuit parameters are  $R=500 \Omega$ ,  $C=100 \text{ pF}$ , and  $I_{co}=2.3 \mu\text{A}$ , which corresponds to  $L_{J_0}=0.1 \text{ nH}$ . The  $Q$  of the simulated circuit is about 500. (b) A plot of  $L_J(\Phi_{ext})$  given by Eq. (9) for different values of  $\beta$ . The circular markers represent the inflection points where  $d^2 L_J / d\Phi^2$  is zero. The illustration shows that depending on the dc flux bias, the ac modulation of  $L_J$  due to  $\Phi_{ac}$  can result in a lower ( $\Phi_{dc}=0.5\Phi_0$ ) or higher ( $\Phi_{dc}=0$ ) effective inductance.

The nonlinear behavior of the simulated LRC circuit is due to an ac flux drive. In particular, the nonlinear inductor is mutually coupled to an external flux bias of  $\Phi_{ext}=\Phi_{dc}+\Phi_{ac}$ , where  $\Phi_{dc}$  models the dc flux bias that was applied experimentally to the SQUID, and  $\Phi_{ac}$  models the ac flux drive that was mutually coupled to the SQUID from a nearby loop. In reality, we expect that the induced flux due to the circulating current in the resonating loop was coupled to the SQUID. The coupled flux became significant especially near the resonant frequency at which the resonating current is enhanced by the quality factor  $Q$ . In the simulations, the ac flux drive is given by  $\Phi_{ac}=\alpha\Phi$ , where it is proportional to the self-induced flux of the inductor  $\Phi$  and has the same frequency as the driving frequency  $\omega_s$ .

The dynamics of the nonlinear LRC circuit is governed by Eq. (6) with

$$h = \frac{\Phi}{L_J(\Phi_{ext})}. \quad (10)$$

Assuming that  $(1-\beta^2)/(1+\beta^2) \ll 1$ , Eq. (10) can be expanded in the form of  $a\Phi+b\Phi^2+c\Phi^3$ , where  $b \sim \sin(2\pi\Phi_{dc}/\Phi_0)$  and  $c \sim \cos(2\pi\Phi_{dc}/\Phi_0)$ . For the cases

when  $\Phi_{dc}=0$  or  $\Phi_{dc}=0.5\Phi_0$ ,  $b=0$ . The resulting equation is of the form of a Duffing equation with both a linear and cubic term in  $\Phi$ . With increasing drive, there will be a bending of the resonant frequency with its associated hysteresis.<sup>34</sup> Moreover, the sign of the cubic term is opposite for  $\Phi_{dc}=0$  and  $\Phi_{dc}=0.5\Phi_0$ , and hence bending will be in opposite directions, as needed to qualitatively explain the data. At intermediate values of  $\Phi_{dc}$  there will be a competition between the quadratic and cubic terms. Finally, it should be noted that for small coupling ( $\alpha \approx 0$ ), Eq. (10) reduces to a linear inductance, which depends on  $\Phi_{dc}$  in a sinusoidal-like fashion.

The circuit parameters used for the simulations were  $C=100 \text{ pF}$ , and  $I_{co}=2.3 \mu\text{A}$ , corresponding to  $L_{J_0} \sim 0.1 \text{ nH}$ . The choice of  $C$  and  $L_{J_0}$  were based on best estimates of the actual sample parameters. In the actual sample, the quality factor  $Q$  was based on the transformed value of the  $50 \Omega$  load with the tapped-inductor network. On the other hand, the resistance  $R$  in the simulated circuit was chosen to give a desirable quality factor  $Q$ . The simulation results presented here were based on  $R=500 \Omega$  which corresponds to a  $Q$  of 500. Moreover, the coupling parameter  $\alpha$  was chosen such that  $\Phi_{ac}$  was about  $0.1\Phi_0$  near the resonant frequency.

Given that the tapped-inductor network was not included in the simulated circuit, i.e., we have kept the nonlinear inductor  $L_J$  based on the best estimate of the SQUID parameters and omitted the bias inductor  $L_s$ , i.e.,  $L_2$  in Fig. 1(b), we expected the simulation results to be quantitatively different from the experimental data in two ways: First, the resonant frequency of the simulated response will be higher; and second, the resultant amount of bending in the nonlinear resonant spectrum given by  $\delta f$  in Eq. (7) will be larger.

By numerically solving Eq. (6) for  $\Phi$  at different driving frequencies  $\omega_s$ , the magnitude and phase spectra of the voltage across the inductor  $V_L=d\Phi/dt$  were obtained. In Fig. 8 the spectra are shown for increasing drive amplitude for  $\Phi_{dc}=0, 0.3\Phi_0$ , and  $0.5\Phi_0$ .  $V_L$  is plotted in reduced units of  $\Phi_0/\sqrt{L_{J_0}C}$ , and the drive amplitude  $I$  is in units of  $2I_{co}$ . The driving frequency was swept such that the lower stable branch within the bistable region is shown for all flux biases. The simulation qualitatively resembles the experimental data presented in Fig. 3. As expected, the nonlinear spectrum has a lower resonant frequency at  $\Phi_{dc}=0$ , and a higher resonant frequency at  $\Phi_{dc}=0.5\Phi_0$ . Also, discontinuities are observed at the boundary of the bistable region for the higher biases. At  $\Phi_{dc}=0.3\Phi_0$ , the magnitude spectra at the two highest input biases exhibit two discrete jumps, one at a lower frequency when the magnitude is increasing, and another at a higher frequency when the magnitude is decreasing. As for the phase spectra, a partial phase drop occurs at the low-frequency discontinuity, while most of the phase drop occurs at the high-frequency discontinuity.

The hysteretic behavior was also captured with the simulations and shown in Fig. 9. This was performed by stepping the driving frequency in both the low-to-high and high-to-low frequency directions, and by ensuring the initial conditions used for the next frequency point were the solutions obtained for the previous frequency point. We have assumed that the square of the drive amplitude  $I^2$  for the simulations is proportional to the input power for the experiment.

The top row of plots in Fig. 9 shows the typical simulated hysteretic behavior at various flux biases for  $I/2I_{co}=0.01$ .

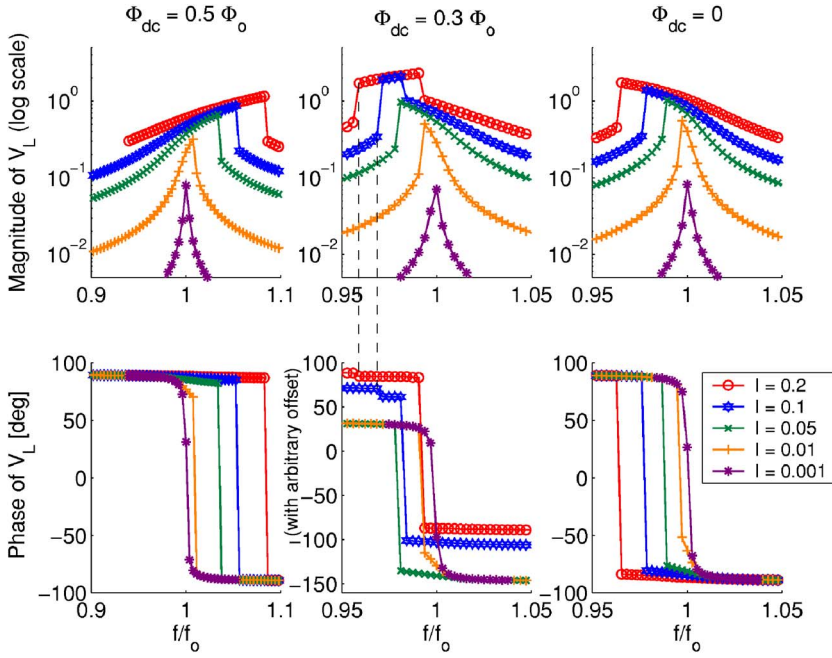


FIG. 8. (Color online) Simulated magnitude and phase spectra of  $V_L$  for increasing drive amplitude  $I$ . The results qualitatively reproduce the experimentally observed behavior in Fig. 3.  $V_L$  is plotted in reduced units of  $\Phi_o/\sqrt{L_{Jo}C}$  and  $I$  in units of  $2I_{co}$ . The frequency axes are normalized with respect to the resonant frequency of the linear spectrum:  $f_o=1.88$  GHz ( $\Phi_{dc}=0$ ), 1.59 GHz ( $0.3\Phi_o$ ), and 1.33 GHz ( $0.5\Phi_o$ ). The phase spectra at the highest drives  $I=0.1$  and  $0.2$  for  $\Phi_{dc}=0.3\Phi_o$  are arbitrarily shifted for display purpose.

The extent of the bistable region given by  $|\delta f_t - \delta f_b|$  is the largest at  $\Phi_{dc}=0.5\Phi_o$  for this drive amplitude. The middle and bottom rows of plots show the dependence of  $\delta f_b$  and  $\delta f_t$  as a function of input power, and resonance-peak power, respectively. The trend at  $\Phi_{dc}=0.3\Phi_o$  shows a qualitative resemblance to the experimental data. The magnitude of  $\delta f_t$  initially increases linearly with the power of the drive for

$\Phi_{dc}=0$  and  $0.5\Phi_o$  similar to the data. As explained previously, this linear dependence is expected at low drives due to the nature of the nonlinearity.<sup>34,36</sup>

It has been discussed earlier that the omittance of the bias resistor in the resonating loop from the actual circuit was expected to cause discrepancy in the simulated values for the resonant frequency and  $\delta f$ . With reference to Eq. (5), the

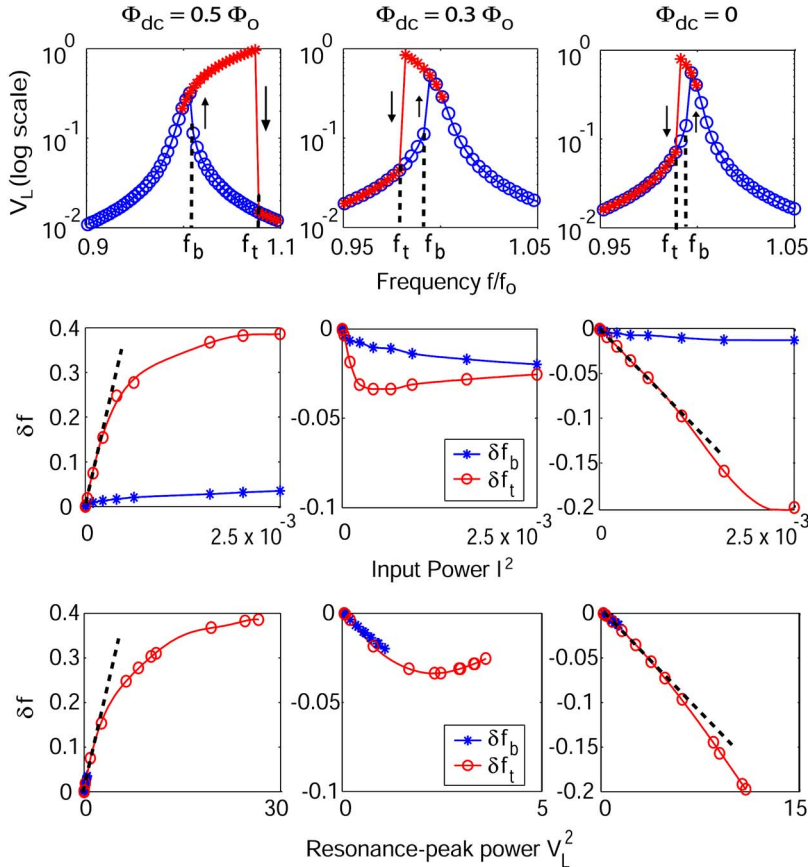


FIG. 9. (Color online) Top row: simulated hysteretic behavior at various flux bias for drive amplitude  $I=0.01$ . Middle row:  $\delta f_b$  and  $\delta f_t$  as a function of the square of the drive amplitude, which is proportional to the input power. The simulations were performed for  $I$  between 0.001 and 0.05. Bottom row:  $\delta f_b$  and  $\delta f_t$  as a function of the square of the voltage response  $V_L$ , which is proportional to the resonance-peak power.  $V_L$  is in reduced units of  $\Phi_o/\sqrt{L_{Jo}C}$  and  $I$  is in units of  $2I_{co}$ .

effect of a bias inductor was estimated with a linear analysis using  $L_s=1.4$  nH. This estimate results in the resonant frequency reduced to 419 MHz while  $\delta f$  was also reduced to about  $10^{-4}$ , consistent with the data.

Finally, we have performed simulations with higher values of  $R$ , which correspond to  $Q=1000$  and  $5000$ . As  $Q$  increased, we observed that the resonance-peak voltage/current was enhanced when the circuit was driven in the linear regime, but the enhancement effect decreased at higher input drive and was negligible in the strongly nonlinear regime. Similarly,  $\delta f$  increased with  $Q$  in the weakly nonlinear regime, but the effect became negligible in the strongly nonlinear regime.

The nonlinear LRC circuit model presented here is meant to show the qualitative trends in the data. To be more quantitative, we have analyzed more complex circuits.<sup>29</sup> For example, we have considered the current-driven circuit across an asymmetric SQUID with self-inductance, and mutual inductive coupling between the SQUID loop and the resonating loop. The simulation results reproduced the data with reasonable numbers; however, the quantitative fitting of the data was not possible due to the uncertainty in the actual on-chip values for the capacitances and the mutual or self-inductances.

## VI. DISCUSSION

In this paper, we experimentally characterized the nonlinear resonant behavior of the readout circuit to be utilized in a resonant scheme for measuring a PC qubit. Different levels of nonlinearity in the readout operation were demonstrated by varying the level of input bias to the circuit. Given the high-quality factor of the resonance, we observed unique manifestation of the nonlinearity due to the Josephson inductance of the readout SQUID. The resonant spectrum of the

readout circuit became asymmetric in the nonlinear regime, and the polarity of the asymmetry changed sign as a function of dc magnetic flux bias to the SQUID. The numerical simulations based on a nonlinear LRC circuit model qualitatively reproduced the trends in the experimental data.

To perform time-resolved measurements of the qubit on a microsecond time scale, the resonant readout is to be operated at a bias frequency  $f_s$  near the resonant frequency  $f_o$ . The change in the resonant frequency due to the qubit signal is thus detected as a difference in the magnitude or phase of the output voltage at  $f_s$ .

While operating the resonant readout in the linear regime keeps the input bias low and reduces the level of decoherence on the qubit, the readout operated in the nonlinear regime has the advantage of being used as a bifurcation amplifier.<sup>24</sup> In particular, the bias frequency  $f_s$  can be chosen within the bistable region of the nonlinear spectrum such that the system has two stable solutions corresponding to different voltages. The probability of occupancy in the higher (lower) stable solution is sensitive to changes in the resonant frequency  $f_o$  (qubit-mediated) relative to  $f_s$ , and provides additional sensitivity for qubit readout over the linear approach.

## ACKNOWLEDGMENTS

We thank Daniel Oates, Yang Yu, Jonathan Habif, and Sergio Valenzuela for useful discussions, and Terry Weir for technical assistance. This work was supported in part by AFOSR Grant No. F49620-01-1-0457 under the DURINT Program, and by the Laboratory for Physical Sciences, and by NSF. The work at Lincoln Laboratory was supported by the U.S. Department of Defense under Air Force Contract No. F19628-00-C-0002.

\*Present address: EECS Department, MIT.

- <sup>1</sup>Y. Makhlin, G. Schön, and A. Shnirman, *Rev. Mod. Phys.* **73**, 357 (2001).
- <sup>2</sup>J. Clarke, A. N. Cleland, M. H. Devoret, D. Esteve, and J. H. Martinis, *Science* **239**, 992 (1988).
- <sup>3</sup>J. R. Friedman, V. Patel, W. Chen, S. K. Tolpygo, and J. E. Lukens, *Nature (London)* **406**, 43 (2000).
- <sup>4</sup>C. H. van der Wal, A. C. J. ter Haar, F. K. Wilhelm, R. N. Schouten, C. J. P. M. Harmans, T. P. Orlando, S. Lloyd, and J. E. Mooij, *Science* **290**, 773 (2000).
- <sup>5</sup>Y. Nakamura, Yu. A. Pashkin, and J. S. Tsai, *Nature (London)* **398**, 786 (1999).
- <sup>6</sup>I. Chiorescu, Y. Nakamura, C. J. P. M. Harmans, and J. E. Mooij, *Science* **299**, 1869 (2003).
- <sup>7</sup>T. Kutsuzawa, H. Tanaka, S. Saito, H. Nakano, K. Semba, and H. Takayanagi, *Appl. Phys. Lett.* **87**, 073501 (2005).
- <sup>8</sup>B. L. T. Plourde, T. L. Robertson, P. A. Reichardt, T. Hime, S. Linzen, C.-E. Wu, and John Clarke, *Phys. Rev. B* **72**, 060506(R) (2005).
- <sup>9</sup>Y. Yu, S. Han, X. Chu, S. Chu, and Z. Wang, *Science* **296**, 889 (2002).
- <sup>10</sup>J. M. Martinis, S. Nam, J. Aumentado, and C. Urbina, *Phys. Rev. Lett.* **89**, 117901 (2002).
- <sup>11</sup>D. Vion, A. Aassime, A. Cottet, P. Joyez, H. Pothier, C. Urbina, D. Esteve, and M. H. Devoret, *Science* **296**, 886 (2002).
- <sup>12</sup>I. Chiorescu, P. Bertet, K. Semba, Y. Nakamura, C. J. P. M. Harmans, and J. E. Mooij, *Nature (London)* **431**, 159 (2004).
- <sup>13</sup>A. Wallraff, D. I. Schuster, A. Blais, L. Frunzio, R.-S. Huang, J. Majer, S. Kumar, S. M. Girvin, and R. J. Schoelkopf, *Nature (London)* **431**, 162 (2004).
- <sup>14</sup>J. Johansson, S. Saito, T. Meno, H. Nakano, M. Ueda, K. Semba, and H. Takayanagi, *Phys. Rev. Lett.* **96**, 127006 (2006).
- <sup>15</sup>W. D. Oliver, Y. Yu, J. C. Lee, K. K. Berggren, L. S. Levitov, and T. P. Orlando, *Science* **310**, 1653 (2005).
- <sup>16</sup>M. Sillanpää, T. Lehtinen, A. Paila, Yu. Makhlin, and P. Hakonen, *Phys. Rev. Lett.* **96**, 187002 (2006).
- <sup>17</sup>D. M. Berns, W. D. Oliver, S. O. Valenzuela, A. V. Shytov, K. K. Berggren, L. S. Levitov, and T. P. Orlando, *Phys. Rev. Lett.* **97**, 150502 (2006).
- <sup>18</sup>Yu. A. Pashkin, T. Yamamoto, O. Astafiev, Y. Nakamura, D. V.

- Averin, and J. S. Tsai, *Nature (London)* **421**, 823 (2003).
- <sup>19</sup>A. J. Berkley, H. Xu, R. C. Ramos, M. A. Gubrud, F. W. Strauch, P. R. Johnson, J. R. Anderson, A. J. Dragt, C. J. Lobb, and F. C. Wellstood, *Science* **300**, 1548 (2003).
- <sup>20</sup>T. Yamamoto, Yu. A. Pashkin, O. Astafiev, Y. Nakamura, and J. S. Tsai, *Nature (London)* **425**, 941 (2003).
- <sup>21</sup>A. Lupascu, E. F. C. Driessen, L. Roschier, C. J. P. M. Harmans, and J. E. Mooij, *Phys. Rev. Lett.* **96**, 127003 (2006).
- <sup>22</sup>M. Grajcar, A. Izmailkov, E. Il'ichev, Th. Wagner, N. Oukhanski, U. Hübner, T. May, I. Zhilyaev, H. E. Hoenig, Ya. S. Greenberg, V. I. Shnyrkov, D. Born, W. Krech, H.-G. Meyer, Alec Maassen van den Brink, and M. H. S. Amin, *Phys. Rev. B* **69**, 060501(R) (2004).
- <sup>23</sup>A. Wallraff, D. I. Schuster, A. Blais, L. Frunzio, J. Majer, M. H. Devoret, S. M. Girvin, and R. J. Schoelkopf, *Phys. Rev. Lett.* **95**, 060501 (2005).
- <sup>24</sup>I. Siddiqi, R. Vijay, M. Metcalfe, E. Boaknin, L. Frunzio, R. J. Schoelkopf, and M. H. Devoret, *Phys. Rev. B* **73**, 054510 (2006).
- <sup>25</sup>B. Abdo, E. Segev, O. Shtempluck, and E. Buks, *Phys. Rev. B* **73**, 134513 (2006).
- <sup>26</sup>C. C. Chin, D. E. Oates, G. Dresselhaus, and M. S. Dresselhaus, *Phys. Rev. B* **45**, 4788 (1992).
- <sup>27</sup>J. E. Mooij, T. P. Orlando, L. Levitov, L. Tian, C. van der Wal, and S. Lloyd, *Science* **285**, 1036 (1999).
- <sup>28</sup>T. P. Orlando, J. E. Mooij, L. Tian, C. H. van der Wal, L. Levitov, S. Lloyd, and J. J. Mazo, *Phys. Rev. B* **60**, 15398 (1999).
- <sup>29</sup>J. C. Lee, Ph. D. thesis, MIT, 2006.
- <sup>30</sup>C. Bowick, *RF Circuit Design* (Newnes Press, Boston, MA, 1982).
- <sup>31</sup>K. Berggren, E. Macedo, D. Feld, and J. Sage, *IEEE Trans. Appl. Supercond.* **9**, 3271 (1999).
- <sup>32</sup>J. C. Lee, W. D. Oliver, T. P. Orlando, and K. K. Berggren, *IEEE Trans. Appl. Supercond.* **15**, 841 (2005).
- <sup>33</sup>Steven H. Strogatz, *Nonlinear Dynamics and Chaos* (Addison-Wesley, Reading, MA, 1994).
- <sup>34</sup>A. H. Nayfeh and D. T. Mook, *Nonlinear Oscillations* (Wiley, New York, 1979).
- <sup>35</sup>F. Kouril and K. Vrba, *Non-linear and Parametric Circuits, Principles, Theory and Applications* (Wiley, New York, 1988).
- <sup>36</sup>L. D. Landau and E. M. Lifshitz, *Mechanics* (Pergamon, New York, 1960).
- <sup>37</sup>A. Barone and G. Paterno, *Physics and Applications of the Josephson Effect* (Wiley, New York, 1982).
- <sup>38</sup>T. Holst and J. Bindslev Hansen, *Physica B* **165-166**, 1649 (1990).